High-resolution shape model of Ceres from stereophotoclinometry using Dawn Imaging Data

R.S. Park[a],[*], A.T. Vaughan[a], A.S. Konopliv[a], A.I. Ermakov[a], N. Mastrodemos[a], J.C. Castillo-Rogez[a], S.P. Joy[a], A. Nathues[b], C.A. Polanskey[a], M.D. Rayman[a], J.E. Riedel[a], C.A. Raymond[a], C.T. Russell[c], M.T. Zuber[d]

[a] *Jet Propulsion Laboratory, California Institute of Technology, Pasadena, CA 91109, USA*
[b] *Max Planck Institute for Solar System Research, Goettingen, Germany*
[c] *Department of Earth, Planetary, and Space Sciences, University of California, Los Angeles, CA 90095-1567, USA*
[d] *Department of Earth, Atmospheric and Planetary Sciences, Massachusetts Institute of Technology, Cambridge, MA 02139, USA*

ARTICLE INFO

ABSTRACT

We present a high-resolution global shape model of Ceres determined using the stereophotoclinometry technique developed at the Jet Propulsion Laboratory by processing Dawn's Framing Camera data acquired during Approach to post-Low Altitude Mapping Orbit (LAMO) phases of the mission. A total of about 38,000 images were processed with pixel resolutions ranging from 35.6 km/pixel to 35 m/pixel and the final global shape model was produced with 100-m grid spacing. The final SPC-derived topography was computed relative to the (482 km, 482 km, 446 km) mean ellipsoid, which ranges from -7.3 km to 9.5 km. For the purpose of validation, we performed various error analyses to assess and quantify realistic uncertainties in the derived topography, such as dividing the data into different subsets and re-computing the entire topography. Based on these studies, we show that the average total height error of the final global topography model is 10.2 m and 88.9% of the surface has the total height error below 20 m. We also provide improved estimates of several physical parameters of Ceres. The resulting GM estimate is (62.62905 ± 0.00035) km^3/s^2, or the mass value of $(938.392 \pm 0.005) \times 10^{18}$ kg. The volume estimate is $(434.13 \pm 0.50) \times 10^6$ km^3 with a volumetric mean radius of 469.72 km. Combined with the mass estimate, the resulting bulk density is (2161.6 ± 2.5) kg/m^3. Other improved parameters include the pole right ascension, $\alpha_0 = (291.42763 \pm 0.0002)°$, pole declination, $\delta_0 = (66.76033 \pm 0.0002)°$, and prime meridian and rotation rate of $(W_0 = 170.309 \pm 0.011)°$ and $(dW/dt = 952.1532635 \pm 0.000002)$ deg/day, respectively. Also, for geophysical and geological studies, we provide spherical harmonic coefficients and a gravitational slope map derived from the global shape model.

1. Introduction

The Dawn spacecraft entered into orbit around the dwarf planet Ceres in March 2015 after exploring Vesta in 2011–2012, becoming the first spacecraft to orbit two solar system bodies other than Earth. One of Dawn's primary science goals at Ceres was to obtain its global shape/topography, which can be used to determine and to characterize many geophysical properties of Ceres (Russell et al., 2006; Konopliv et al., 2011; Raymond et al., 2011) and to derive constraints on its internal evolution. For example, geophysical findings based on Dawn's imaging data, combined with gravity data, showed that Ceres is nearly in hydrostatic equilibrium with isostatically compensated topography and with a volatile-rich shell (Park et al., 2016; Ermakov et al., 2017; Fu et al., 2017; Konopliv et al., 2017). An accurate topography model is also important for photometric correction of images used in geologic analysis of surface features (Nathues et al., 2017; Schröder et al., 2017), as well as for geomorphologic analysis (e.g., Buczkowski et al., 2012).

Prior to the Dawn mission, the best images of Ceres were from the Hubble Space Telescope (HST) with about 30-km resolution (Thomas et al., 2005). Dawn's Framing Camera (FC) (Sierks et al., 2011), with the pixel resolution of 93.7 μrad/pixel, exceeded the HST resolution in late-January 2015 as the spacecraft approached Ceres. The best image resolution used in the current study comes from the Low Altitude Mapping Orbit (LAMO) with pixel scale of about 35-m/pixel at an average altitude of about 380 km. The time span of the Dawn imaging data considered in this study started on February 4, 2015, just after

---

[*] Corresponding author.
E-mail address: Ryan.S.Park@jpl.nasa.gov (R.S. Park).

Table 1
Dawn Framing Camera image dataset processed to determine the global shape model of Ceres. A total of 38,056 images was processed with the best image pixel scale of about 35 m/pixel during the LAMO phase. The FC pixel resolution is 93 μrad per pixel. The last column shows the fractional Ceres surface coverage by 3 or more images with an illumination angle of less than 80° and an emission angle of less than 60°.

Science Phases	Time of the First Image (UTC)	Time of the Last Image (UTC)	Duration (days)	Number of Images	Pixel Scale (m/pixel)	Fractional Surface Coverage (%)
Approach	2015-JAN-13 20:21:56	2015-MAY-22 23:43:18	129	1089	470–35,600	97.9
Survey	2015-JUN-05 15:29:33	2015-JUN-25 23:02:44	20	863	~410	97.9
HAMO	2015-AUG-18 04:53:42	2015-OCT-21 09:48:54	64	2373	~140	97.9
LAMO	2015-DEC-16 09:27:00	2016-AUG-27 01:38:41	255	33,731	~35	97.4

the time when the image resolution exceeded HST, and ended on August 27, 2016, which is the end of the extended-LAMO phase. The raw images and ancillary files used in this study are available through the Planetary Data System (PDS) Small Body (https://sbn.psi.edu/pds/resource/dawn/dwncfcL1.html) and Navigation and Ancillary Information Facility (NAIF, https://naif.jpl.nasa.gov/pub/naif/DAWN/kernels) nodes. Although not used in this study, the calibrated images are also available through the PDS Small Body Node. Moreover, to date, the only archived and publicly available shape model of Ceres from Dawn is based on High Altitude Mapping Orbit (HAMO) images (Preusker et al., 2016; Roatsch et al., 2016a) with pixel scale of about 140 m/pixel.

In this study, the images acquired by the Dawn spacecraft were processed using the stereophotoclinometry (SPC) technique developed at the Jet Propulsion Laboratory (JPL) (Gaskell 2005; Gaskell et al., 2008; Park et al., 2016) as part of Dawn gravity science investigation. The main objective of Dawn gravity science investigation is to determine the gravitational field, rotational state, ephemeris, and global shape model of Ceres through an iterative process of orbit determination (OD) and SPC (Konopliv et al., 2011, 2017; Park et al., 2016). For most space missions, gravity science relies primarily on radio data through OD; however, there are cases where imaging data would substantially improve the overall quality of gravity science results (Park et al., 2015), and Dawn was a clear case that would benefit from imaging data through landmark tracking (Konopliv et al., 2011, 2017; Park et al., 2016). Since landmarks are the final products of SPC, the global topography computed from SPC naturally became a part of Dawn gravity science investigation. More details on the use of imaging data for gravity science can be found in Section 2. The OD was performed using JPL's two independent software suites, i.e., MIRAGE (Multiple Interferometric Ranging and GPS Ensemble) (Moyer, 1971, 2000) and MONTE (Mission Analysis, Operations, and Navigation Toolkit Environment) (Evans et al., 2018). The SPC software suite used in this study is identical to the one that was used to navigate Dawn, which has been modified and improved over the years from the experience of successfully navigating numerous space flight missions, e.g., Near-Earth Asteroid Rendezvous, Hayabusa-1 and Rosetta. This paper focuses on the SPC side of the overall gravity science investigation. Details of OD and corresponding gravity science results can be found in Park et al. (2016) and Konopliv et al. (2017). Similar studies on Dawn's Vesta gravity science investigation can be found in Konopliv et al. (2014) and Park et al. (2014).

In general, SPC has many similarities to stereo photogrammetry (SPG), a well-established technique for producing topography using stereo pairs of images (Preusker et al., 2016; Roatsch et al., 2016a), such as the need for a large range of image emission angles ranging from nadir to over 40°. However, there are also substantial differences, key among them the need for a large variation in incidence angle in both elevation and azimuth for SPC. With regard to surface topographic reconstruction, assuming each method has optimal image acquisition, to first order they produce comparable global height precision. Moreover, SPC uses control points (also known as landmarks) defined relative to the center of mass which are tied to small topographic maps on the surface that can be used for gravity science investigation by tracking landmarks to improve the spacecraft state knowledge and by solving for

systematic non-gravitational effects (Konopliv et al., 2011, 2017; Park et al., 2016). The association of control points to small-scale topographic maps enables SPC to be used effectively for real-time navigation when processing new images, with a quick turnaround (i.e., a few hours) in a mostly automated fashion. Additionally, SPC can make effective use of images with a wide range of surface resolutions. Typically, a factor of ten between the highest and lowest resolution is acceptable to the software process, allowing for more images that contribute to the topographic model and a long data arc for OD that can even span multiple mission phases.

2. Ceres shape determination process

2.1. Imaging data and orbit geometry

The Dawn spacecraft is equipped with a primary (FC2) and a back-up (FC1) framing camera with the instantaneous field of view (iFOV) of 93.7 μrad/pixel and the field of view (FOV) of $5.5° \times 5.5°$ (Sierks et al., 2011); the FC2 camera was used throughout the Dawn mission and yielded the data arcs used in this study. Table 1 shows the duration, number of images, and pixel resolution of the acquired clear-filter images during each science phase. The orbit altitude for each science phase was ~13,500 km for Approach, ~4390 km for Survey, ~1470 km for HAMO and ~380 km for LAMO. Although the highest image resolution and the best gravity data come from the LAMO phase (i.e., lowest altitude considered in this study), higher altitude data are also used since they are helpful for determining long-wavelength features of the Ceres shape. Low-resolution images from early mission phases were also used to develop the initial shape model, which was iteratively refined in subsequent mission phases, such that all of the imagery has a contribution to the final shape model. These images have a pixel scale ranging from 35.6 km to 35 m. Specifically, the image data from Approach and Survey phases were used to construct an *a priori* shape model of Ceres with a few kilometers pixel scale that was the basis of the HAMO shape model (i.e., landmark locations and maps for later iterations). The direct contribution of these early low-resolution images to the final Ceres shape model was negligible and were not used in the final SPC iteration. The final shape model was produced only using the data acquired during HAMO to post-LAMO phases. The HAMO phase was divided into 6 imaging cycles. Each imaging cycle allowed a complete coverage of the visible surface of Ceres. Two of these cycles were pointed in the nadir direction and the other four cycles were pointed in fixed off-nadir directions. Two of the off-nadir directions were chosen to give optimum imaging geometry for SPC and the other two for SPG although all four were used by both methods. It is worth noting that the large azimuth and elevation variations that are optimal for SPC were absent due to the sun-synchronous design of the orbits. During the LAMO phase the camera was mostly pointed in the nadir direction, making the image resolution strictly dependent on the altitude although there was some range in the incidence angle.

2.2. Stereophotoclinometry

An accurate shape model is essential for understanding the geophysical nature of Ceres. Using FC images acquired during all science

phases of the Ceres mission through LAMO, an SPC technique was applied to construct a high-precision, three-dimensional shape model of Ceres, i.e., surface heights relative to Ceres' center of mass. By matching images to the model, the same SPC process provides the data needed for the OD and determination of landmark positions, which are crucial for determining Ceres global parameters (e.g., spin-pole axis, rotation rate, etc.). The use of SPC-derived landmark data is further discussed in Section 2.3.

Unlike conventional stereo methods, which utilize parallax in overlapping images to extract height information, the photoclinometry method makes use of brightness and shading variations in images with unique illumination and view angles. This approach makes the assumption that surface brightness variations are associated with viewing angle and topography; when images contain considerable brightness variation associated with surface unit composition, this translates to a source of error in the recovery of height. Using multiple images with unique illumination angles, the SPC method can solve for slopes and 'relative' albedos for terrain in the overlapping regions. The result is a set of high-resolution surface height and relative albedo maps covering the imaged, illuminated surface. As can be seen in the last column of Table 1, we have better than 97% surface coverage in all mission phases by 3 or more images with an incidence angle of less than 80° and an emission angle of less than 60°. Although the imaging campaign was not fully optimized for SPC, the coverage indicated in Table 1 was sufficient to produce a model with the uncertainty demonstrated in Section 2.4.

The mapping process began with an *a priori* shape model that was a simple tri-axial ellipsoid with the primary axes of (487.3 km, 487.3 km, 454.7 km) (Thomas et al., 2005). A set of low-resolution maps was created to tile the surface in the regions with sufficient image coverage, with the map commensurate with the early image resolution. In the SPC process, a "map" is an array of $N \times N$ grid points, where each grid point contains the local height and albedo values. Each map also includes a body-fixed control vector to the center of a reference plane (i.e., origin at the center of mass), a body-relative orientation, and the spatial extent of each grid cell that we call the 'map scale', which is essentially the ground sample distance (GSD). The first maps that were created had a map scale of ~ 2.5 km, while image data taken in the Approach phase of the mission had an image pixel scale that decreased from about 8 km/pixel to about 1.3 km/pixel. For each new mission phase, when sufficient data is available at a higher resolution than the previous set, a new set of maps was generated by tiling the surface in longitudinal bands. The overlap between neighboring maps was targeted to be approximately 30% in both the longitude and latitude directions. The scale of each set of new maps was selected such that the scale ratio between new and old maps was approximately less than a factor of 3, and the same between the new map scale and the new image resolution. The highest resolution maps achieved in this model were constructed from HAMO and LAMO data and had a map scale of 100 m. Approximately 64,000 individual maps at 100 m map scale are required for complete coverage of the body, including partial overlap between maps that is essential to tie neighboring maps together.

To make these initial maps, an overlapping grid of maps was established, where each map was defined by latitude and longitude (eastward) values formulated to achieve the desired overlap fraction. Then for each map, a set of images that meet certain criteria were selected. These criteria include the fraction of the illuminated part of the image that is included in the map area, minimum and maximum range in the ratio between image scale and map grid spacing, and minimum and maximum in the emission angle at the center of the map. For images that met these criteria, the part of each image that overlapped the map, was extracted, resampled to the map grid scale, and ortho-projected onto the pre-existing topographic model, which at that point was the *a priori* shape model. Each image was visually inspected prior to inclusion in the model. Saturated images – those where all or most of the pixels representing Ceres were at their maximum value – were discarded. In particular, we did not include in the height solution the

over-exposed images acquired by the navigation team for the purpose of a star-based pointing solution. Images with high phase angles were initially included and processed but were evaluated in the model and later discarded if they consistently failed to register with any maps, especially with higher resolution maps that were created later. Registration outliers between image data and existing maps were addressed individually, requiring manual adjustments to provide a better *a priori* location for the automated process.

Once the set of images that cover a given map have been collected and ortho-rectified, the existing landmark heights were rendered under the same camera and illumination angles as the individual pictures. The illumination function for image k is (Gaskell 2005; Gaskell et al., 2008):

$$I_k(x) = \Lambda_k a(x) R(\cos i, \cos e, \alpha) + \Phi_k, \qquad (1)$$

where x is the set of map locations and $a(x)$ is the relative albedo at location x. The set of albedos a is normalized such that expected value of the albedo array is 1. The scaling term Λ_k and the bias term Φ_k are solved for each picture using a least-squares fit over the extracted, ortho-rectified image data. The general reflectance model is a combination of Lambert and Lomell–Seeliger reflectance functions (Hapke, 1981; Squyres and Veverka, 1982; McEwen, 1986; Fairbairn, 2005),

$$R(\cos i, \cos e, \alpha) = (1 - L(\alpha)) \cos i + \frac{L(\alpha) \cos i}{\cos i + \cos e}. \qquad (2)$$

Here i and e are the angles of incidence and emission, respectively, with respect to the surface normal at map location x. The values $\cos i$ and $\cos e$ can be computed directly from the slope information stored internally for map location x. For Ceres, we used a phase-free variant of Eq. (2) by fixing $L(\alpha) = 0.65$. This value was chosen because it provided consistent global shape, orbit, and gravity solutions, which was checked extensively by comparing independent solutions from the gravity science team, orbit determination team, and SPC team. We also note that varying $L(\alpha)$ at a few percent level, or using a different reflectance function (e.g., Minnaert), would cause the reconstructed shape of Ceres to vary less than the formal error. Detailed statistical comparisons are shown in Section 2.4.

Subsequently, the slopes and relative albedo are estimated, at each map pixel, via a weighted least-squares process that minimizes the difference between the extracted brightness template and the predicted morel brightness, $I_k(x)$, while also solving for the scale and bias terms, Λ_k and Φ_k. In general the surface-projected images are subject to various systematic and stochastic errors, such as camera position errors, camera pointing errors and rotational frame errors, and as such, especially in the early stages, they are not aligned with each other within the same map. Once the slopes and albedo within a map have been solved for, the brightness templates are cross-correlated with the mean brightness model so they are all aligned to each other to a very high accuracy, often less than 0.01 map pixels. A few iterations between the slope/albedo estimation step and the cross-correlation step as usually sufficient to minimize the brightness residuals.

Once the slope and albedo estimation has converged, the height for each map pixel is then estimated using an iterative least-squares fit at each map pixel, solving for the slopes and albedos necessary to model the extracted image data across all of the views.

The estimated slope solution is integrated into map heights using a second iterative process. The height at map location x, denoted $h(x)$, can be computed according to:

$$h(x) = \frac{\sum \left(h(x + \delta x_k) - \delta x_k \cdot (t(x) + t(x + \delta x_k))/2 \right) + w_c h_c(x)}{w_c + 4}. \qquad (4)$$

Here, the subscript k indicates each of the 4 directions on the map grid, surrounding the point of interest. The summation subscript has been omitted for clarity, but the sum is over all k, meaning all surrounding map locations. Eq. (4) is a calculation of the height of the map point in direction k, offset by the change in height that results from projecting back towards the point of interest along the *average* slope of

the kth point and the central point. This projected height is summed over all directions, with the addition of the current height, $h_c(x)$, weighted by w_c, which is typically very small, i.e., on the order of 1%. The term in the denominator creates a weighted average, since there are slope-based height estimates from the four directions, and the central height with weight w_c. In implementation, there are provisions for edge cases and missing heights.

The process described in Eq. (4) is iterated many times across the entire map in a pseudorandom order. The slopes $t(x)$ and $t(x + \delta x_k)$ come from the surface height solution, and for the initial iteration the heights are seeded at random map post locations, using data from a variety of user-selected sources and a coverage fraction provided by the user. In particular, it is common to use existing map heights, heights from neighboring maps, and heights from the shape model to constrain the slope-to-height integration.

As a result of the slope estimation and height integration across the overlapping network of individual maps, a piecemeal shape model is established over all regions of the body with sufficient coverage. The individual maps consist of a body-fixed control vector that establishes the absolute heights (i.e., relative to Ceres center of mass), and a grid of heights relative to the map plane. A 'global solution' accounts for the location of the landmarks in the image data, the overlaps between neighboring landmarks, and how the landmarks present as limb profiles in the images. The collection of maps is then merged into an implicitly connected quadrilateral (ICQ) global shape model, which is used internally and can be exported and converted to other formats for use by gravity science and others. Additionally, the maps are simulated under the illumination conditions of each picture that they are present in. Correlation between the rendered map and the rectified image data provides the pixel/line location of the landmark control vector in the image frame, which is passed to OD as an observable. Section 3 describes the stereophotoclinometry-derived products archived from this study.

2.3. Global iteration

The main error sources for SPC are the uncertainties in the camera position and camera pointing direction, which are difficult to separate. This is mainly because the image data alone are not sensitive for determining the radial position of the camera. Also, it is difficult to identify systematic errors in the long-wavelength topographic variation when combining maps to create global three-dimensional shape. SPC can make discrete corrections to camera position (and pointing as well); however, these discrete corrections would be dynamically incorrect since spacecraft position cannot change instantaneously. We resolve these errors by combining the optical data with radio data to better constrain the spacecraft and landmark positions through an OD process (Park et al., 2016; Konopliv et al., 2017). The Doppler data measure the line-of-sight velocity of Dawn relative to a Deep Space Network (DSN) station extremely accurately, which is very sensitive to the radial distance, especially for low altitudes. We make dynamically consistent corrections to the camera position by estimating the initial spacecraft state so that the integrated trajectory would yield correct camera position at the time of imaging. This technique provides more power constraints and leads to a better solution than solving for discrete corrections to the camera position.

In the OD process, where we process both optical and radio data, we estimate the spacecraft state, camera pointing direction, gravity field, rotational parameters, landmark positions, and various parameters related to spacecraft non-gravitational forces and measurement calibrations. For example, Fig. 1 shows the corrections made to camera boresight direction for each image, where the boresight direction is defined as the direction normal to the camera focal plane. The correction to the boresight direction is typically less than 2 pixels with a mean of ~0.7 pixel. Note that we actually estimate three angles that define the full camera frame relative to the inertial frame through OD, but we

only show the boresight direction since it's easy to visualize and the corrections along other camera frame directions show similar level of variations. These corrections are mainly due to the thermal fluctuations in the Framing Camera boresight direction and the errors in the reconstructed spacecraft orientation from star trackers.

Once the OD solution is converged, the camera position, camera pointing direction, and landmarks are passed on to SPC and the steps given in Section 2.2 are repeated until some convergence criterion is satisfied. Note that the camera position is essentially the spacecraft position (i.e., camera is fixed in the spacecraft frame). The camera position and camera pointing values from OD are then held fixed in SPC; only the landmark positions are estimated in SPC. In other words, SPC does not estimate camera position and camera pointing direction.

It is important to emphasize that the local solutions within each map, i.e., map slopes, albedo and heights, landmark vector, camera pointing, and camera position, are inter-dependent and each iteration improves upon each other. A corrected camera position vector and landmark vector improve the projection of the images on the map, thereby increasing the accuracy of the extracted brightness template. The corrected camera vector improves the predicted brightness model and the slope/albedo solution, which in turn allows for more accurate local height estimation. Also, the cross-correlation between the observed and predicted brightness model shifts each landmark in the image frame, adjusting the optical observables that in turn improved the OD.

Overall, global shape determination is an iterative process of SPC and OD until both the SPC and OD solutions converge, and we note that it is crucial to combine both processes to minimize potential systematic errors. Our process allows SPC to incorporate the latest camera position, camera pointing, and landmark solutions from OD in each iteration so that corrections are dynamically consistent.

Since both OD and SPC estimate the landmarks, a good measure for checking the consistency between OD and SPC is the level of corrections that OD makes given landmark positions from SPC. Fig. 2 shows the total landmark corrections made by OD. We note that this difference is substantially improved, on the order of tens of meters to a few meters, compared to what was presented in Konopliv et al. (2017), mainly due to performing additional iterations between OD and SPC that resulted in a more optimal solution.

We should note that the SPC processes described in Sections 2.2 and 2.3 are two essential uses for the technique. The local SPC process produces topography in the individual maps using algorithms that are dependent on the reflectance model, in this analysis defined by Eq. (2). This process is robust to variation in illumination across the source images, but subject to errors stemming from assumptions about the photometric model. For the global solution, the SPC process is used to align renders of the map topography with the image data, and these observations are used in the OD solution. This is essentially a bundle adjustment solution with SPC-derived observations, and since the render of the maps is performed with the same photometric model that was used to originally derive the topography, we expect this matching to be largely independent of variations in the reflectance model. The global solution is geometric, robust, and well understood, with rigorous error analysis of the sort that is presented in Fig. 3. The local solution and its vulnerability to changes in the photometric model is less well understood, however we have attempted to address this with the study of an alternative model in Section 2.4.

2.4. Topography height error analysis

After sufficient iteration between SPC and OD, the final output of SPC is a cloud of landmark points represented as 3-dimensional body-fixed vectors and landmark maps. The landmark points are tied to the Ceres center of mass and they define the global shape of Ceres. The landmark maps are used to create a merged shape model as discussed in Section 2.2.
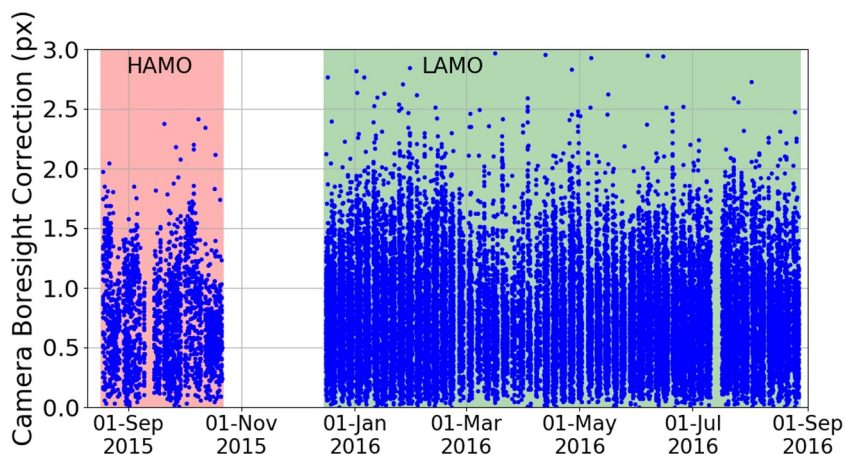
Fig. 1. Corrections made to camera boresight direction through a global orbit determination process during the HAMO phase shown in the left (red) and the LAMO phase shown in the right (green). The correction is typically less than 2 pixels with a mean of ∼0.7 pixel, which is mainly due to the thermal fluctuations in the Framing Camera boresight and the errors in the reconstructed spacecraft orientation from star trackers. Camera boresight corrections made during Approach and Survey phases are similar to, but generally smaller than, HAMO and LAMO corrections. The gap in the middle is when the Dawn spacecraft thrusted to lower its altitude and no images were acquired.

In general, there are two types of errors in this global SPC-derived shape in radial direction: *inertial* and *relative* errors. Note that the radial direction is different from the direction normal to the (482 km, 482 km, 446 km) mean ellipsoid, along which the heights are computed. The maximum angular difference is ≈ 4° at a latitude of ≈ 45°. The maximum relative difference between radial and ellipsoid-normal errors is only 0.25%. Since this difference is small, we use the radial shape error as a useful approximation of the topographic height error.

The center of each map (described in Section 2.2) is called the landmark vector or control point, which is essentially a fixed point on Ceres' surface relative to the center of mass, and we call the error in the landmark vectors the *inertial* error, mainly because it is tied to the inertial camera position and inertial camera pointing errors. The SPC process provides a network of landmarks and their locations in the images, and these are used to triangulate the position of the spacecraft. Since landmarks are typically observed multiple times, it is possible to estimate landmark locations as a part of global OD process. Specifically, the landmark locations were estimated together with spacecraft state, camera pointing direction, Ceres gravity field, Ceres spin-pole direction, Ceres rotation rate, non-gravitational forces, etc. Since orbit determination is based on a least-squares principle, it is straightforward to quantify errors in the estimated landmark locations (i.e., from the estimated covariance matrix) with respect to Ceres center of mass. Fig. 3(top) shows the *inertial* uncertainty in the estimated landmark radial height, where the variations are due to spacecraft orbit geometry and accuracy as well as solar illumination conditions. The average inertial height error is 8.6 m, which is based on an area-weighted average using 100-m grid. A total of 91.4% of the global surface had the inertial height error below 20 m.

The *relative* error is defined by how accurately neighboring maps overlap. This depends solely on SPC and it is typically less than the *inertial* error. Several analyses were performed to quantify the relative uncertainty in the SPC process. During routine creation and processing of the maps that make up a complete model, there is overlap between neighboring maps. The overlaps between maps are a requirement for continuity of the model, allowing neighboring maps to seed absolute heights from each other and providing a correlation measure that contributes to the overall geometric shape solution. In regions where two or more maps overlap, there is a redundant solution for that given patch of surface that has been derived independently for multiple maps using similar data sets. An uncertainty value can be computed in these areas that gives a quantitative measure of the self-consistency of SPC. An arbitrary query point that penetrates two independent maps should result in similar height values from each map, and the variation between overlapping maps arises from small data differences between the maps, nonlinearities at the map edges, small spatial offsets between the maps, and interpolation error. Fig. 3(middle) shows the *relative* uncertainty in the topography height. The average relative height error

(area-weighted) of the global topography is 4.6 m and 97.8% of the surface had the relative height error below 20 m.

To further validate the relative error statistics, we have performed additional studies. An alternate method of quantifying the relative uncertainty is to divide the data (i.e., spacecraft imagery) into discrete sets and reprocess the entire model. For example, in regions where the surface coverage is sufficient, a given map could be rebuilt two times: once with one half of the data, and again with the other half of the data. This analysis results in two maps of the same patch of surface, constructed of completely independent data sets and using separate instances of the process. Once each map has been rebuilt independently, the two models can be differenced point-by-point at the full map resolution, resulting in a data set of hundreds of millions of points. Some deviation between rebuilt maps is to be expected, since a random halving of the data set makes no provision for the quality of the data that remains. The SPC method performs best when the surface patch is viewed under multiple illumination conditions, so the arbitrary data selection will weaken the data quality unless coverage of the region is very redundant. We must also be wary of outliers when processing half a billion data points, as single points that slip into shadow between the two data sets, or other subtle edge cases, can result in large singular deviations that are not representative of the set. We did not manually or automatically clip these outliers, so they remain as multi-sigma outliers in the formal standard deviation calculation used for the results below.

This type of "split model" analysis was performed for a variety of approaches to dividing the data. The first approach was to divide the data such that 'every-other' picture went into one model or the other. A second approach divided the data "by time," such that the first half of HAMO and the first half of LAMO went into one model, and the second half of each phase went into the other model. The purpose of this approach is to attempt to identify any time-dependent biases in the images themselves or the ancillary data, such as time, attitude, or rotation frame kernels. A third approach was to reprocess one model with only HAMO data, and another with only LAMO data, with heights seeded from the unified final model.

In general, we find that the split-model analysis is consistent with the relative error analysis previously described and shown in Fig. 3(middle). When dividing the picture data 'every-other', we compute a *whole-model* mean difference between the two cases of only 0.004 m, indicating that there is no bias when different data sets of the same body are processed in the same way through SPC. The standard deviation of the differences across the entire body is 7.5 m under this approach. When dividing the data by time, we find a global mean difference of 0.26 m, with a formal standard deviation of 11.70 m. We should note that no outlier rejection was performed in these analyses; this is a formal standard deviation across the entire body, including the poles.

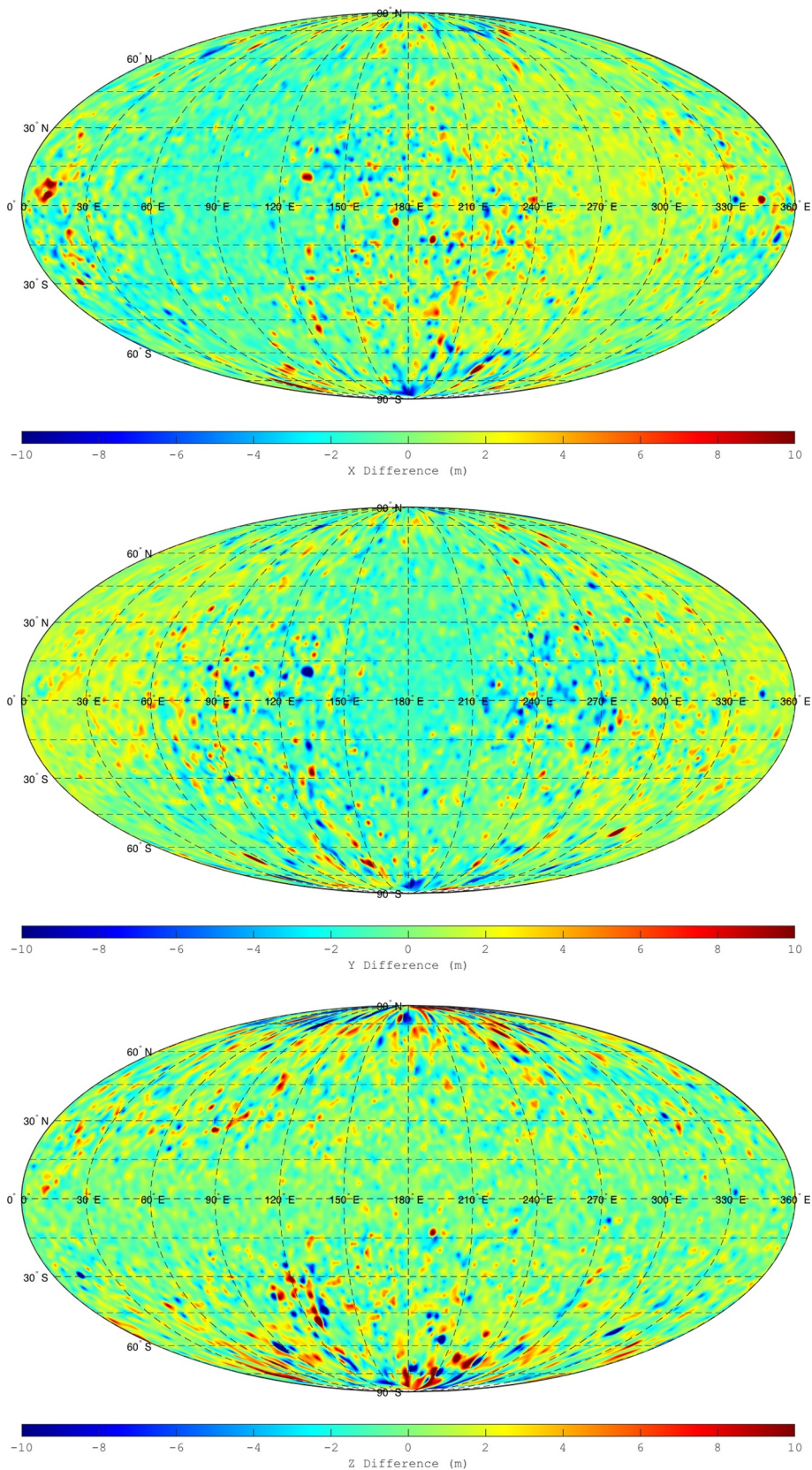The case of dividing the data between HAMO and LAMO proved

Fig. 2. Differences in the landmark solutions between the SPC and OD (i.e., global gravity solution) in Ceres body-fixed X (top), Y (middle), and Z (bottom) coordinates. These are essentially identical to the plots shown in Konopliv et al. (2017), Fig. 15, but shows much improved consistency between SPC and OD landmark solutions.
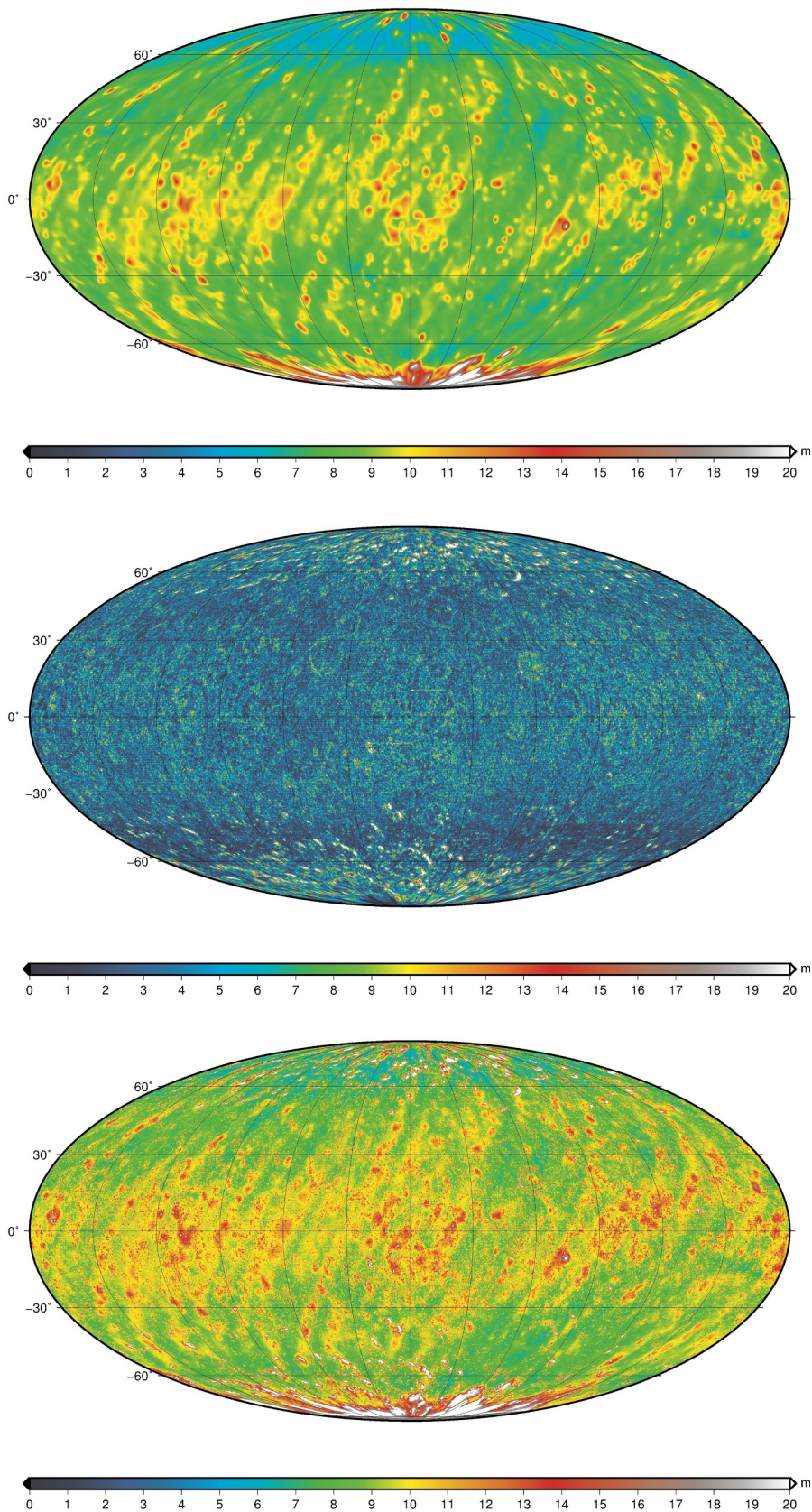
Fig. 3. Top: shows the inertial height uncertainty (i.e., height uncertainty in the estimated landmarks). The average inertial height error is 8.6 m and about 91.4% of the surface has the inertial height error below 20 m. Middle: shows the relative height uncertainty (i.e., error from map correlation). The average relative height error is 4.6 m and about 97.8% of the surface has the relative height error below 20 m. Bottom: shows the root-sum-square of inertial and relative uncertainties (i.e., total topography height error). The average total height error is 10.2 m and about 88.9% of the surface has the total height error below 20 m. In all figures, vertical lines represent the longitude lines for every 30° increment and the middle vertical line represents the 180° East longitude line.

more difficult to analyze. There are significant regions of the surface where data coverage changes substantially between the two mission phases. In these areas, reprocessing a landmark with insufficient coverage in some areas results in relatively large changes in the heights.

The SPC software process does not fail, but the heights in regions of insufficient coverage are interpolated from lower-resolution underlying models, resulting in a height difference that is not representative of the body at large, due to coverage limitations. The simple solution to this
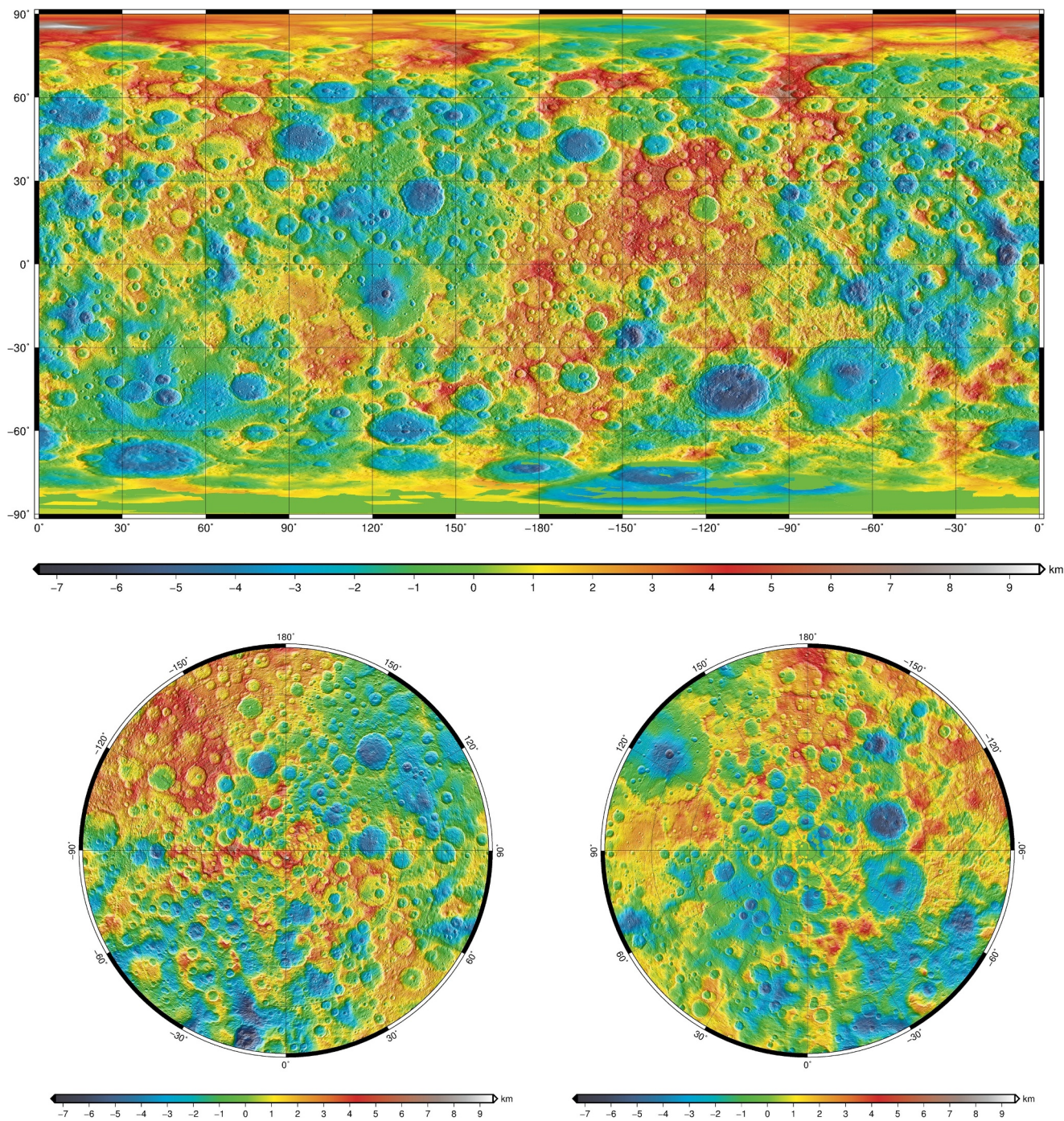
Fig. 4. The cylindrical equidistant projection of SPC topography (top), stereo projection of the Northern hemisphere (bottom left), and stereo projection of the Southern hemisphere (bottom right). The horizontal map resolution is 100 m and the topography is computed relative to the (482 km, 482 km, 446 km) mean ellipsoid. The global topography height ranges from −7.3 km to 9.5 km.

issue is to limit the analysis to regions where the coverage was similar for both phases. For example, if we restrict the analysis to ± 40° of latitude, we find a global mean difference of 0.14 m, with a formal standard deviation of 11.71 m. This is nearly the same result we achieved when reconstructing the model using half of each mission phase, in the 'half by time' case above.

We have also performed a full model reconstruction with an alternate reflectance function, to provide some perspective on the sensitivity of the topography to changes in the model. We have implemented the Minnaert model referenced in Schröder, et al. (2017) for Ceres for comparison with the Lambert/Lomell–Seeliger model. We rebuilt the

full set of maps from the source imagery using the Minnaert model. Since a full iteration with OD would slightly shift the landmarks so that we cannot do a 1:1 difference between the new map and old map heights, we differenced Lambert/Lomell–Seeliger model from the Minnaert model on a per-map basis. This approach focuses on the standard deviation of the radial differences for each map as an indication of the scale of the variation between the two models. The average of the 1-sigma standard deviation across all of the approximately 64,000 rebuilt maps is 17.0 m. The average of all of the individual maps' mean radial differences is 0.35 m. In general, the height difference of a 2-dimensional longitude/latitude map showed 1-sigma
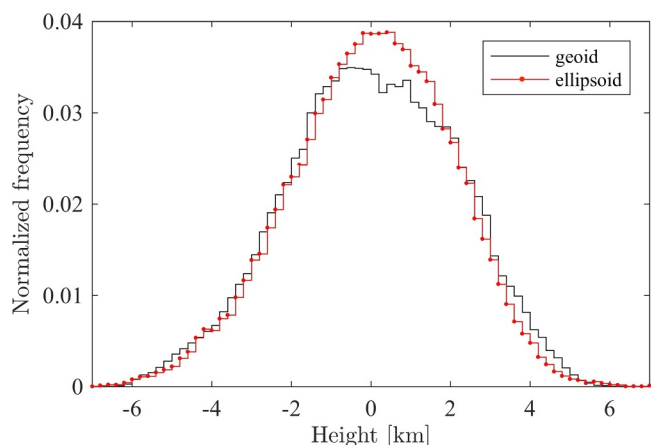
Fig. 5. The histogram of heights (hypsogram) with respect to the reference ellipsoid with dimensions (482 km, 482 km, 446 km) (red with filled circles) and equipotential surface or geoid (black). The Ceres' hypsograms are unimodal and nearly symmetric. About 90% of heights with respect to the reference ellipsoid is between −3.4 and 3.2 km. About 90% of heights with respect to geoid is between −3.5 and 3.4 km.

standard deviation with slightly higher differences for the regions with rapid slope change, such as crater rims.

Given the inertial and relative errors, we compute the *total* height error by computing the root-sum-square of the two errors, i.e., $\sqrt{\sigma_I^2 + \sigma_R^2}$, where σ_I and σ_R represent inertial error and relative error, respectively. Fig. 3(bottom) shows the *total* height error, which can be considered as the realistic height error in the SPC-derived topography with 100 m GSD. The average total height error is 10.2 m and 88.9% of the surface had the total height error below 20 m. If we consider more conservative statistics by summing the inertial and relative errors, the resulting average height error is 13.1 m and 84.3% of the surface had the total height error below 20 m. In either case, Dawn mission's requirement of obtaining a topographic map of 80% of the surface with horizontal resolution of 200 m and vertical resolution of 20 m is well satisfied (Rayman et al., 2006).

3. Stereophotoclinometry-derived science products

3.1. Ceres shape products

The SPC-derived global shape models of Ceres are archived through PDS. Specifically, we have archived ICQ global shape models and gridded shape models with map scale of 300 m and 100 m through the PDS NAIF node (NAIF, https://naif.jpl.nasa.gov/pub/naif/DAWN/kernels/dsk/), along with ancillary files such as spacecraft ephemeris, camera pointing, Ceres spin-pole axis, prime meridian, and rotation rate (i.e., Planetary Constants Kernel, PCK), etc.

Fig. 6. An example of a single map from the Ceres model rendered under the illumination conditions of two spacecraft images. The center of this particular map is at the center of the Kait crater (see the black arrow). The map has a grid spacing of 100 m, and a size of 99 grid points on a side (thus each square is 9.9 km on a side). The top row shows image data from two FC2 images: FC2_00042363 from HAMO (top left) at approximately 135 m/pixel, and FC2_00083036 from LAMO (top right) at approximately 35 m/pixel. The bottom row shows the map rendered under the illumination conditions of the image above it. Note that the image data in the top row has been sampled onto the grid spacing of the map.

Fig. 4 shows the topography of Ceres, where the height is computed relative to the plane that is normal to the (482 km, 482 km, 446 km) mean ellipsoid, in cylindrical equidistant projection (top), stereographic projection of the northern hemisphere (bottom left), and stereographic projection of the southern hemisphere (bottom right). The global topography map ranges from −7.3 km to 9.5 km. We note that an ellipsoid is used as the vertical reference for heights (datum), the maps shown in Fig. 4 are based on projections of a sphere and the use of planetocentric coordinates.

Fig. 5 shows the histogram of the topography shown in Fig. 4, which is unimodal and nearly symmetric. About 90% of the heights with respect to the reference ellipsoid is between −3.4 and 3.2 km. Fig. 5 also shows the hypsogram with respect to a geoid (i.e., equipotential surface) for a comparison purpose. About 90% of the heights with respect to the geoid is between −3.5 and 3.4 km.

3.2. Ceres physical properties

Since SPC and OD are iterated until both solved-for parameters have converged, the final SPC shape model is tied to the overall gravity

Table 2
Ceres spin pole, prime meridian and rotation rate solutions. Subsequent to the publication of the Ceres gravity products in Konopliv et al. (2017), we have made additional iterations of stereophotoclinometry and orbit determination leading to small corrections to the *GM* estimate. The difference in the *GM* solution from previous results (Konopliv et al., 2017) is due to the improvement in the Ceres shape model, which removed a systematic error in the *GM*. Also, the pole right ascension, pole declination, prime meridian, and rotation rate are slightly improved as well.

Solution	GM (km³/s²)	α_0 (deg)	δ_0 (deg)	W_0 (deg)	dW/dt (deg/day)
Thomas et al. (2005), Chamberlin et al. (2007) (pre-Dawn)	62.7 ± 0.8	291 ± 5	59 ± 5	170.9	952.1532 ± 0.0002
Park et al. (2016)	62.6284 ± 0.0009	291.421 ± 0.007	66.758 ± 0.002	170.65	N/A
Konopliv et al. (2017)	62.62736 ± 0.00040	291.42744 ± 0.00022	66.76065 ± 0.00022	170.311 ± 0.012	952.153264 ± 0.000002
This paper	62.62905 ± 0.00035	291.42763 ± 0.00020	66.76033 ± 0.00020	170.309 ± 0.011	952.1532635 ± 0.000002

Note: the standard value of G was updated somewhere between the first gravity field release (i.e., Park et al., 2016 used $G = 6.67384 \times 10^{-20}$ km³/(s²·kg) Mohr et al., 2012) and the current publication. Using the latest value of $G = 6.67408 \times 10^{-20}$ ·km³/(kg·s²) Mohr et al., 2016), the resulting Ceres mass is $(938.392 \pm 0.005) \times 10^{18}$ kg.
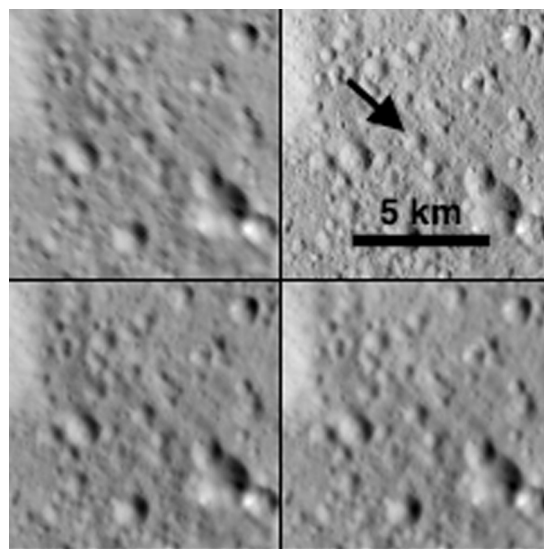
Table 3

Various best-fitting ellipsoid estimates of the global shape of Ceres in the Ceres body-fixed coordinate system with origin at the center of mass. Here, a_e, b_e and c_e represent the three principal semi-axes, θ_e, ϕ_e and ψ_e represent the orientation angles of the principal axes, and c_x, c_y and c_z represent the coordinates of the ellipsoid center. The result for fitting all nine parameters is shown in the first row, which is the best-fitting model for geophysical interpretation. The second case is the result of fitting semi-axes and ellipsoid center. The third case is fitting the semi-axes and ellipsoid orientation parameters. The last two cases are fitting an ellipsoid or a spheroid that would be useful for reducing astrometry data. The RMS_e column shows the root-mean-square error of each fit. Overall, there is an improvement of about 100-m in estimating the orientation or the center of the ellipsoid.

Cases	a_e (km)	b_e (km)	c_e (km)	θ_e (deg)	ϕ_e (deg)	ψ_e (deg)	c_x (km)	c_y (km)	c_z (km)	RMS_e (km)
Ellipsoid with orientation and center	483.21	481.00	445.93	127.223	89.188	−80.454	−0.93	−0.35	0.36	1.81
Ellipsoid with center	482.17	482.03	445.94	0.000	90.000	0.000	−0.92	−0.34	0.36	1.91
Ellipsoid with orientation	483.21	481.00	445.93	127.208	89.190	−80.433	–	–	–	1.91
Ellipsoid	482.16	482.03	445.94	0.000	90.000	0.000	–	–	–	2.00
Spheroid	482.10	482.10	445.94	0.000	90.000	0.000	–	–	–	2.00

science solution, e.g., spin-pole axis. In theory, all parameters should be within the error bars of the published values in Konopliv et al. (2017); however, the current study has made small changes to a few parameters that are worth noting, mainly because the improved landmark solutions shown in Fig. 2. Table 2 shows the resulting *GM*, pole right ascension, pole declination, prime meridian, and rotation rate. Note that W_0 was chosen such that the small crater on Ceres named Kait defines the 0° longitude position, which is consistent with International Astronomical Union's definition (Roatsch et al., 2016b) (see Fig. 6). This coordinate system is not aligned with the principal axes frame defined by the gravity field. Other global parameters, such as gravity spherical harmonic coefficients, are well within the quoted uncertainties reported in Konopliv et al. (2017).

From the final SPC shape model, the resulting volume of Ceres is $(434.13 \pm 0.50) \times 10^6$ km^3 with volumetric mean radius of 469.72 km. The volume uncertainty is dominated by the regions in the southern hemisphere with no imaging data and the derived uncertainty (i.e., ~0.1%) is an upper bound. This yields the bulk density value of (2161.6 ± 2.5) kg/m^3. The global shape model is defined with respect to the center of mass in body-fixed coordinate frame. The origin is Ceres center of mass mainly because the spacecraft coordinate system (i.e., camera coordinate system) is defined relative to Ceres center of mass. In this coordinate system, the center of figure offset is $(−0.893, −0.379, 0.351) \pm 0.015$ km, or a magnitude of (1.031 ± 0.015) km, and the maximum distance between the center of mass to the surface is 487.03 km (i.e., Brillouin sphere radius).

3.3. Ellipsoidal products

Given a three-dimensional shape model, a best-fit ellipsoid model is often useful for various practical purposes. Table 3 shows several different ways for computing a best-fit ellipsoid. Typically, the best fitting method for geophysical interpretation is where we estimate three semi-principal axes (a_e, b_e, c_e) three principal axes orientation angles (θ_e, ϕ_e, ψ_e), and three-dimensional center of ellipsoid (c_x, c_y, c_z) in the Ceres body-fixed frame, which is co-aligned with the frame where the gravity field is determined. The unit vectors along the three principal axes are defined as:

$$u_a = \begin{bmatrix} +\cos\theta_e \sin\phi_e \cos\psi_e - \sin\theta_e \sin\psi_e \\ +\sin\theta_e \sin\phi_e \cos\psi_e + \cos\theta_e \sin\psi_e \\ -\cos\phi_e \cos\psi_e \end{bmatrix}, \quad u_b = \begin{bmatrix} -\cos\theta_e \sin\phi_e \sin\psi_e - \sin\theta_e \cos\psi_e \\ -\sin\theta_e \sin\phi_e \sin\psi_e + \cos\theta_e \cos\psi_e \\ +\cos\phi_e \sin\psi_e \end{bmatrix}, \quad u_c = \begin{bmatrix} +\cos\theta_e \cos\phi_e \\ +\sin\theta_e \cos\phi_e \\ +\sin\phi_e \end{bmatrix},$$

The result for fitting all nine parameters is shown in Table 3, first row, which would be the best-fitting model for geophysical interpretation. The resulting principal semi-axes are (483.21, 481.00, 445.93) km, which gives a polar flattening of $[(\sqrt{ab} - c)/\sqrt{ab}] = 0.075$, with the ellipsoid major axis along (46.8°E, 0.1°S) direction (Fig. 4) where the topography is high.

The second case in Table 3 is the result of fitting semi-axes and
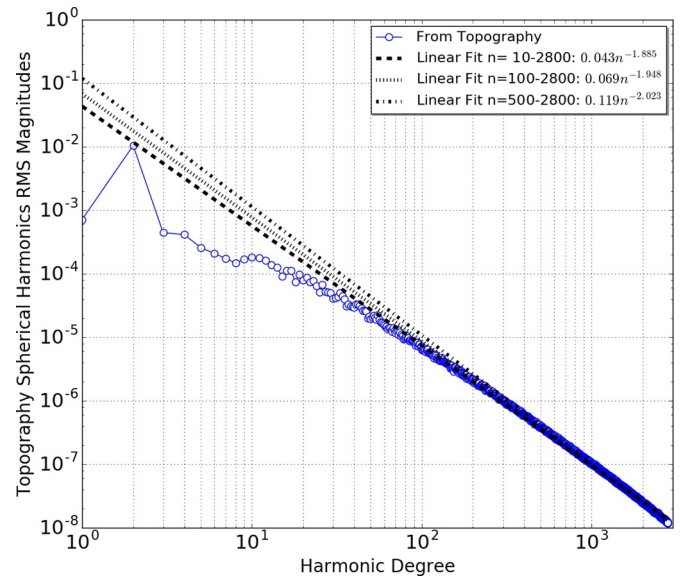
Fig. 7. Root-mean-square magnitudes of the topography spherical harmonics up to degree 2800 computed from integrating over the Ceres global topography (blue line with open circles). Linear fits based on different range of degrees are also provided (black lines).

ellipsoid center. The third case in Table 3 is fitting the semi-axes and ellipsoid orientation parameters. The last two cases in Table 3 are fitting an ellipsoid or a spheroid that would be useful for reducing astrometry data. The RMS_e column shows the root-mean-square error of each fit. Overall, there is an improvement of about 100-m in estimating the orientation or the center of the ellipsoid.

The reference ellipsoid that is typically used to compute topography is the ellipsoid-only case (i.e., Table 3, row 4), which is approximated as (482,482,446) km. While the first case (i.e., nine-parameter fit) would be most useful for geophysical interpretation of Ceres, the last two cases in Table 3 (i.e., ellipsoid-only and spheroid-only) would be useful for reducing future astrometry data to improve the ephemeris of Ceres. This is because astrometry would be taken relative to Ceres center of mass and assuming an ellipsoid or a spheroid would make the data reduction process practically much easier.

Table 4

Topography spherical harmonic coefficients (normalized) derived from the global shape of Ceres up to degree 18, commensurately with the gravity field harmonics.

n	m	$\bar{A}_{nm}$	$\bar{B}_{nm}$	n	m	$\bar{A}_{nm}$	$\bar{B}_{nm}$	n	m	$\bar{A}_{nm}$	$\bar{B}_{nm}$
0	0	9.989E-01	–	10	9	3.666E−05	3.774E−04	15	8	1.122E−04	−6.801E−05
1	0	4.815E−04	–	10	10	3.115E−04	−1.505E−04	15	9	3.555E−05	−1.430E−04
1	1	−1.042E−03	−4.416E−04	11	0	−6.960E−05	–	15	10	2.561E−05	5.681E−05
2	0	−2.330E−02	–	11	1	1.717E−04	2.308E−04	15	11	−1.813E−04	9.550E−05
2	1	3.459E−04	−3.842E−04	11	2	−1.699E−04	3.558E−05	15	12	7.589E−05	−3.286E−05
2	2	−3.866E−05	1.179E−03	11	3	1.547E−04	9.383E−05	15	13	−1.077E−04	2.456E−05
3	0	3.845E−04	–	11	4	1.784E−04	−1.973E−05	15	14	2.809E−05	−3.816E−06
3	1	4.122E−04	1.072E−04	11	5	1.603E−04	−3.080E−04	15	15	−1.054E−05	3.650E−05
3	2	−3.272E−04	9.475E−04	11	6	1.961E−04	−2.849E−05	16	0	4.909E−05	–
3	3	−1.719E−04	−9.192E−05	11	7	−3.364E−04	3.548E−04	16	1	−5.243E−05	−7.444E−05
4	0	9.627E−04	–	11	8	−1.277E−04	−6.866E−05	16	2	−7.863E−05	−3.657E−05
4	1	1.513E−06	4.234E−04	11	9	−1.313E−04	−2.040E−04	16	3	−1.195E−05	−2.016E−04
4	2	3.228E−05	−4.735E−04	11	10	1.201E−04	2.138E−04	16	4	3.096E−06	2.402E−05
4	3	−2.419E−04	−1.702E−05	11	11	−2.234E−05	3.393E−06	16	5	−7.742E−05	−2.054E−05
4	4	3.668E−04	−9.130E−05	12	0	1.597E−04	–	16	6	−2.946E−04	1.666E−04
5	0	9.715E−06	–	12	1	1.982E−04	−3.791E−05	16	7	−6.050E−04	2.788E−05
5	1	8.331E−05	−1.974E−04	12	2	1.933E−04	−2.951E−04	16	8	−1.183E−04	3.458E−05
5	2	−4.438E−04	3.130E−05	12	3	4.115E−05	3.089E−04	16	9	1.463E−04	−1.661E−04
5	3	4.070E−05	−2.181E−04	12	4	1.361E−04	9.704E−05	16	10	1.377E−04	7.771E−06
5	4	−5.323E−04	1.209E−05	12	5	1.825E−05	−2.004E−04	16	11	−1.752E−04	1.114E−04
5	5	−3.561E−04	1.583E−04	12	6	−1.954E−04	−8.001E−05	16	12	−5.530E−05	−1.169E−04
6	0	3.300E−04	–	12	7	−1.987E−04	−6.565E−05	16	13	8.166E−05	−1.630E−04
6	1	−5.043E−05	5.916E−05	12	8	7.230E−05	8.325E−05	16	14	1.128E−04	−5.024E−05
6	2	5.885E−05	5.624E−05	12	9	2.702E−05	8.079E−06	16	15	1.400E−04	−2.188E−06
6	3	−1.370E−05	5.131E−04	12	10	−1.651E−04	−2.229E−04	16	16	2.608E−05	1.494E−04
6	4	1.835E−04	−1.257E−04	12	11	−4.172E−05	−2.682E−04	17	0	1.613E−05	–
6	5	2.818E−04	9.404E−05	12	12	−1.896E−05	−2.449E−04	17	1	2.331E−04	9.460E−05
6	6	−4.824E−05	−1.940E−04	13	0	6.778E−05	–	17	2	5.341E−06	−6.808E−05
7	0	7.502E−05	–	13	1	4.231E−05	−2.584E−05	17	3	8.717E−05	−5.752E−05
7	1	−1.454E−05	5.169E−05	13	2	−6.504E−06	3.840E−06	17	4	4.763E−05	2.229E−05
7	2	3.426E−04	−3.592E−05	13	3	1.213E−04	6.824E−05	17	5	2.679E−04	1.798E−05
7	3	−2.744E−04	−1.018E−04	13	4	−9.328E−05	3.051E−04	17	6	−3.141E−05	1.347E−04
7	4	2.227E−04	−2.230E−04	13	5	−2.122E−04	−7.219E−05	17	7	1.271E−04	1.199E−04
7	5	6.931E−05	−2.908E−04	13	6	−1.408E−04	−1.412E−04	17	8	1.102E−04	−3.679E−06
7	6	−9.924E−06	−2.316E−05	13	7	−1.351E−04	−9.811E−05	17	9	7.141E−07	−5.650E−05
7	7	3.201E−05	−2.331E−04	13	8	−3.877E−04	−1.565E−04	17	10	6.449E−05	−1.329E−04
8	0	9.193E−05	–	13	9	−9.366E−05	−1.062E−04	17	11	−1.723E−04	2.305E−04
8	1	−6.188E−05	8.927E−05	13	10	1.545E−04	−1.107E−04	17	12	−8.856E−05	6.491E−05
8	2	−2.792E−04	5.136E−05	13	11	5.689E−05	−1.296E−04	17	13	−1.169E−04	−1.739E−04
8	3	−2.104E−04	6.323E−06	13	12	−8.172E−05	8.842E−05	17	14	1.787E−04	−1.553E−05
8	4	3.137E−05	1.394E−04	13	13	8.160E−05	3.137E−05	17	15	7.418E−05	3.395E−05
8	5	1.208E−04	−1.888E−05	14	0	6.736E−05	–	17	16	2.897E−05	−1.179E−04
8	6	5.169E−04	−2.365E−04	14	1	−7.732E−05	−1.040E−04	17	17	5.048E−05	−2.154E−05
8	7	−1.509E−04	1.775E−04	14	2	4.928E−05	−3.206E−04	18	0	2.851E−05	–
8	8	2.267E−04	1.457E−04	14	3	7.577E−05	3.048E−04	18	1	1.504E−04	5.705E−05
9	0	1.009E−04	–	14	4	−8.303E−05	−7.464E−05	18	2	−1.538E−05	−5.153E−05
9	1	3.130E−05	3.082E−04	14	5	1.653E−04	−1.205E−04	18	3	2.975E−05	8.858E−05
9	2	2.663E−04	8.643E−05	14	6	−2.927E−05	1.891E−04	18	4	9.045E−05	6.892E−05
9	3	−4.097E−04	−1.619E−05	14	7	5.965E−05	3.947E−05	18	5	2.512E−05	−5.092E−05
9	4	−2.702E−05	5.043E−05	14	8	6.387E−05	−6.044E−05	18	6	−8.862E−05	−1.226E−04
9	5	2.995E−05	−1.844E−04	14	9	8.582E−06	−8.284E−05	18	7	5.020E−05	−4.954E−05
9	6	7.164E−05	−1.337E−04	14	10	−1.202E−04	−1.001E−04	18	8	−4.239E−05	9.679E−05
9	7	−1.465E−04	2.038E−04	14	11	−1.076E−04	−5.829E−05	18	9	−7.154E−05	−3.808E−05
9	8	−5.758E−05	−1.776E−04	14	12	−4.723E−05	−1.412E−04	18	10	2.707E−05	5.770E−05
9	9	1.618E−05	1.686E−04	14	13	−5.657E−05	−6.803E−05	18	11	−1.036E−04	−7.057E−05
10	0	−1.765E−04	–	14	14	1.979E−04	8.010E−05	18	12	4.983E−05	−1.353E−04
10	1	−1.290E−05	−1.308E−04	15	0	−5.142E−06	–	18	13	4.302E−05	2.245E−05
10	2	−6.761E−05	−6.741E−05	15	1	1.348E−04	−4.294E−05	18	14	−6.071E−05	3.229E−05
10	3	4.273E−05	−3.223E−04	15	2	−4.298E−05	−2.427E−04	18	15	2.432E−05	−1.524E−04
10	4	1.618E−04	−5.819E−05	15	3	9.161E−05	1.008E−04	18	16	−1.379E−05	−4.794E−05
10	5	−1.308E−04	−2.560E−04	15	4	1.709E−05	5.427E−05	18	17	9.734E−05	1.036E−05
10	6	−2.927E−04	3.859E−05	15	5	3.114E−05	7.831E−05	18	18	−4.902E−05	−1.266E−04
10	7	−1.268E−04	−9.877E−05	15	6	−1.044E−04	−1.485E−04				
10	8	−1.711E−04	1.055E−04	15	7	6.175E−05	−1.035E−04				

3.4. Topography spherical harmonic coefficients

Given a three-dimensional shape model, a topography spherical harmonic expansion model can be computed through a quadrature method, i.e., integration over the body, which can be represented as:

$$r(\lambda, \phi) = R \sum_{n=0}^{\infty} \sum_{m=0}^{n} \bar{P}_{nm}(\sin \phi)[\bar{A}_{nm} \cos(m\lambda) + \bar{B}_{nm} \sin(m\lambda)],$$

Here, R is the reference radius of Ceres (470 km), $\bar{P}_{nm}$ are the normalized associated Legendre functions, and $\bar{A}_{nm}$ and $\bar{B}_{nm}$ are the normalized topography spherical harmonic coefficients. Note that the reference radius of 470 km is slightly different than the volumetric mean

Table 5
Gravity spherical harmonic coefficients (normalized) derived from the global shape of Ceres assuming a uniform density (i.e., bulk density of 2161.6 kg/m³).

n	m	$\bar{C}_{nm}$	$\bar{S}_{nm}$	n	m	$\bar{C}_{nm}$	$\bar{S}_{nm}$	n	m	$\bar{C}_{nm}$	$\bar{S}_{nm}$
0	0	–	–	10	9	5.498E−06	6.283E−05	15	8	1.733E−05	−2.017E−06
1	0	4.316E−04	–	10	10	5.966E−05	−2.613E−05	15	9	5.907E−06	−1.100E−05
1	1	−1.096E−03	−4.658E−04	11	0	−1.209E−05	–	15	10	−1.391E−06	1.030E−05
2	0	−1.360E−02	0.000E+00	11	1	1.876E−05	1.963E−05	15	11	−1.671E−05	7.934E−06
2	1	2.004E−04	−2.403E−04	11	2	−2.477E−05	1.681E−06	15	12	1.223E−06	−5.907E−06
2	2	−2.465E−05	7.657E−04	11	3	2.525E−05	9.770E−06	15	13	−1.141E−05	4.689E−06
3	0	1.357E−04	–	11	4	2.515E−05	−1.247E−05	15	14	8.494E−07	9.276E−08
3	1	2.033E−04	6.780E−05	11	5	2.487E−05	−3.300E−05	15	15	−2.554E−06	4.767E−06
3	2	−1.240E−04	4.044E−04	11	6	2.547E−05	1.641E−06	16	0	3.062E−06	–
3	3	−7.894E−05	−4.070E−05	11	7	−3.902E−05	4.262E−05	16	1	−4.819E−06	−4.856E−06
4	0	7.287E−04	–	11	8	−7.752E−06	−2.511E−06	16	2	−5.884E−06	5.132E−06
4	1	−9.322E−06	1.436E−04	11	9	−1.810E−05	−2.963E−05	16	3	−4.179E−06	−2.417E−05
4	2	7.008E−06	−1.853E−04	11	10	1.675E−05	3.546E−05	16	4	8.522E−07	2.109E−06
4	3	−8.077E−05	−2.086E−05	11	11	−5.921E−06	1.334E−06	16	5	−1.146E−05	9.025E−07
4	4	1.314E−04	−3.093E−05	12	0	2.031E−05	–	16	6	−2.239E−05	1.137E−05
5	0	−9.969E−06	–	12	1	2.366E−05	3.748E−06	16	7	−3.314E−06	2.836E−06
5	1	5.493E−06	−5.501E−05	12	2	1.927E−05	−2.099E−05	16	8	−1.014E−05	2.525E−06
5	2	−1.160E−04	−1.970E−05	12	3	5.601E−07	3.187E−05	16	9	1.450E−05	−1.288E−05
5	3	2.183E−05	−5.245E−05	12	4	1.299E−05	1.458E−05	16	10	1.439E−05	1.602E−06
5	4	−1.595E−04	9.527E−06	12	5	5.888E−07	−1.356E−05	16	11	−1.294E−05	1.224E−05
5	5	−1.126E−04	5.323E−05	12	6	−1.597E−05	−1.392E−05	16	12	−5.233E−06	−7.522E−06
6	0	1.574E−05	–	12	7	−2.249E−05	−5.331E−06	16	13	8.898E−06	−1.696E−05
6	1	−8.478E−06	−5.861E−06	12	8	9.764E−06	9.759E−06	16	14	1.142E−05	−6.227E−06
6	2	2.035E−05	2.696E−05	12	9	3.299E−06	−3.265E−06	16	15	1.708E−05	7.602E−07
6	3	8.028E−06	1.135E−04	12	10	−2.317E−05	−2.776E−05	16	16	3.088E−06	2.128E−05
6	4	3.541E−05	−3.104E−05	12	11	−5.965E−06	−3.974E−05	17	0	1.013E−06	–
6	5	6.985E−05	2.287E−05	12	12	−2.615E−06	−3.809E−05	17	1	1.343E−05	5.351E−06
6	6	−1.241E−05	−4.956E−05	13	0	9.700E−06	–	17	2	−1.784E−06	−1.808E−06
7	0	1.065E−05	–	13	1	−3.678E−06	−6.046E−06	17	3	9.571E−06	−4.777E−06
7	1	−4.721E−06	7.717E−06	13	2	5.456E−06	3.799E−06	17	4	1.640E−06	1.336E−06
7	2	6.652E−05	−7.258E−06	13	3	4.431E−06	1.186E−06	17	5	1.556E−06	6.226E−07
7	3	−4.192E−06	−1.218E−05	13	4	−1.473E−05	2.944E−05	17	6	−7.994E−07	1.269E−05
7	4	5.808E−05	−4.444E−05	13	5	−2.490E−05	−3.187E−06	17	7	8.683E−06	9.049E−06
7	5	1.922E−05	−5.810E−05	13	6	−1.626E−05	−1.017E−05	17	8	−1.138E−06	−4.675E−06
7	6	−3.948E−06	−3.691E−06	13	7	−8.594E−06	−1.542E−05	17	9	−1.729E−06	8.758E−07
7	7	8.433E−06	−5.862E−05	13	8	−4.309E−05	−1.465E−05	17	10	2.337E−06	−1.166E−05
8	0	1.556E−05	–	13	9	−9.444E−06	−6.147E−06	17	11	−1.202E−05	1.860E−05
8	1	−7.105E−06	1.759E−05	13	10	1.587E−05	−1.785E−05	17	12	−9.913E−06	8.822E−06
8	2	−4.366E−05	5.643E−06	13	11	1.001E−05	−1.739E−05	17	13	−9.256E−06	−1.727E−05
8	3	−3.599E−05	−2.960E−06	13	12	−1.381E−05	1.306E−05	17	14	1.892E−05	−2.988E−06
8	4	−1.340E−06	2.707E−05	13	13	1.141E−05	4.693E−06	17	15	9.304E−06	2.268E−06
8	5	1.934E−05	2.046E−06	14	0	−2.609E−07	–	17	16	4.696E−06	−1.386E−05
8	6	1.525E−05	−4.225E−05	14	1	−9.437E−06	−7.319E−06	17	17	6.829E−06	−3.736E−06
8	7	−2.805E−05	3.722E−05	14	2	1.535E−06	−2.077E−05	18	0	−5.064E−07	–
8	8	5.101E−05	2.892E−05	14	3	6.539E−06	2.397E−05	18	1	9.568E−06	7.020E−06
9	0	1.430E−05	–	14	4	−1.051E−05	−9.600E−06	18	2	−1.554E−07	−4.614E−06
9	1	3.458E−07	3.301E−05	14	5	1.733E−05	−6.796E−06	18	3	5.868E−06	1.253E−05
9	2	3.063E−05	1.203E−05	14	6	7.445E−06	1.586E−05	18	4	4.380E−06	2.654E−06
9	3	−5.525E−05	−1.719E−06	14	7	9.817E−06	4.424E−06	18	5	4.286E−06	−1.211E−06
9	4	−1.444E−05	1.520E−05	14	8	6.867E−06	−7.914E−06	18	6	1.507E−06	−1.126E−05
9	5	−2.628E−06	−1.489E−05	14	9	−2.226E−06	−5.833E−06	18	7	3.199E−06	−2.532E−06
9	6	6.819E−06	−2.034E−05	14	10	−1.225E−05	−8.004E−06	18	8	−1.642E−06	8.734E−06
9	7	−1.813E−05	3.110E−05	14	11	−9.000E−06	−4.995E−06	18	9	−7.573E−06	5.244E−07
9	8	−7.979E−06	−3.202E−05	14	12	−5.683E−06	−1.439E−05	18	10	−1.613E−06	3.411E−07
9	9	2.673E−06	3.617E−05	14	13	−7.579E−06	−7.710E−06	18	11	−6.211E−06	−6.361E−06
10	0	−2.846E−05	–	14	14	2.790E−05	1.133E−05	18	12	2.782E−06	−5.366E−06
10	1	−5.797E−06	−1.819E−05	15	0	−2.693E−06	–	18	13	2.949E−06	5.983E−06
10	2	−5.622E−06	−1.554E−06	15	1	5.416E−06	−3.925E−06	18	14	−7.376E−06	1.334E−06
10	3	1.046E−05	−4.629E−05	15	2	−3.145E−06	−1.838E−05	18	15	7.501E−07	−1.582E−05
10	4	1.687E−05	−1.325E−05	15	3	2.124E−06	8.789E−06	18	16	−6.289E−07	−5.760E−06
10	5	−1.989E−05	−3.062E−05	15	4	3.949E−06	−2.973E−06	18	17	1.125E−05	2.377E−06
10	6	−3.715E−05	1.290E−05	15	5	2.265E−06	6.725E−06	18	18	−6.973E−06	−1.742E−05
10	7	−1.338E−05	−1.540E−05	15	6	−5.265E−06	−1.287E−05				
10	8	−3.058E−05	1.483E−05	15	7	4.571E−06	−7.808E−06				

radius of 469.72 km. While the volumetric mean radius is a physical parameter (i.e., derived from volume), the reference radius used in topography spherical harmonics expansion (or in gravity spherical harmonics expansion) is only used as a scaling parameter. Therefore, it is much more important to use a consistent value, which is why the reference radius value was fixed during the Survey phase and it has not been updated in order to avoid any potential confusion. The normalized spherical harmonic coefficients are related to the un-normalized spherical harmonic coefficients as $(\bar{A}_{nm}, \bar{B}_{nm})N_{nm} = (A_{nm}, B_{nm})$, where the normalization factor N_{nm} is defined as:

$$N_{nm} = \sqrt{\frac{(2 - \delta_{0m})(2n + 1)(n - m)!}{(n + m)!}}.$$

Here, δ_{0m} represents the Kronecker delta function. For example, for
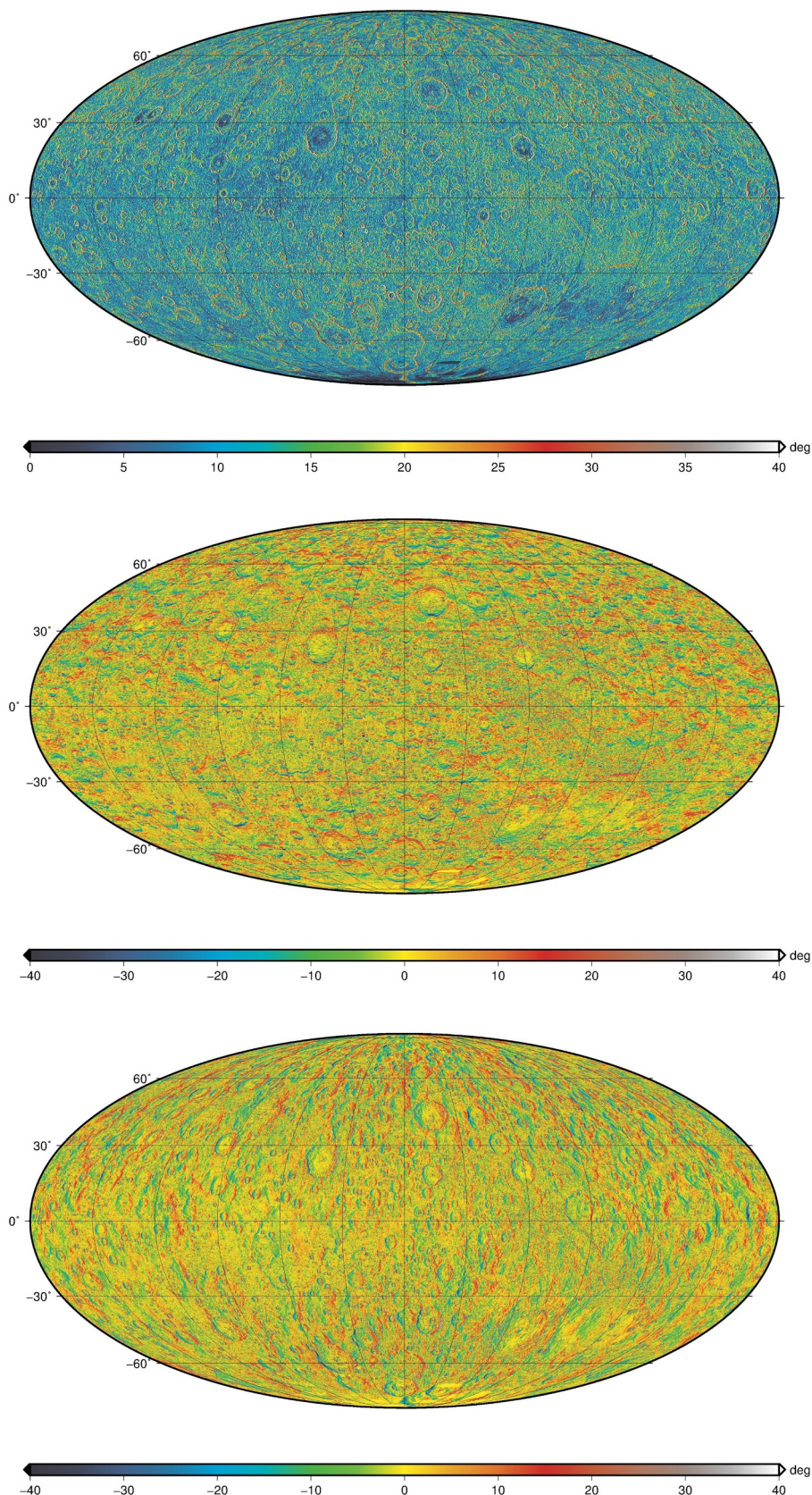
Fig. 8. Total gravitational slope of Ceres topography (top), which is defined as the angle between the inward-pointing surface normal and the sum of the local gravity and centrifugal acceleration vectors. The middle and bottom figures show the North-South and East-West bidirectional gravity slopes, respectively. In all figures, the vertical lines represent the longitude lines for every 30° increment and the middle vertical line represents the 180° East longitude line.
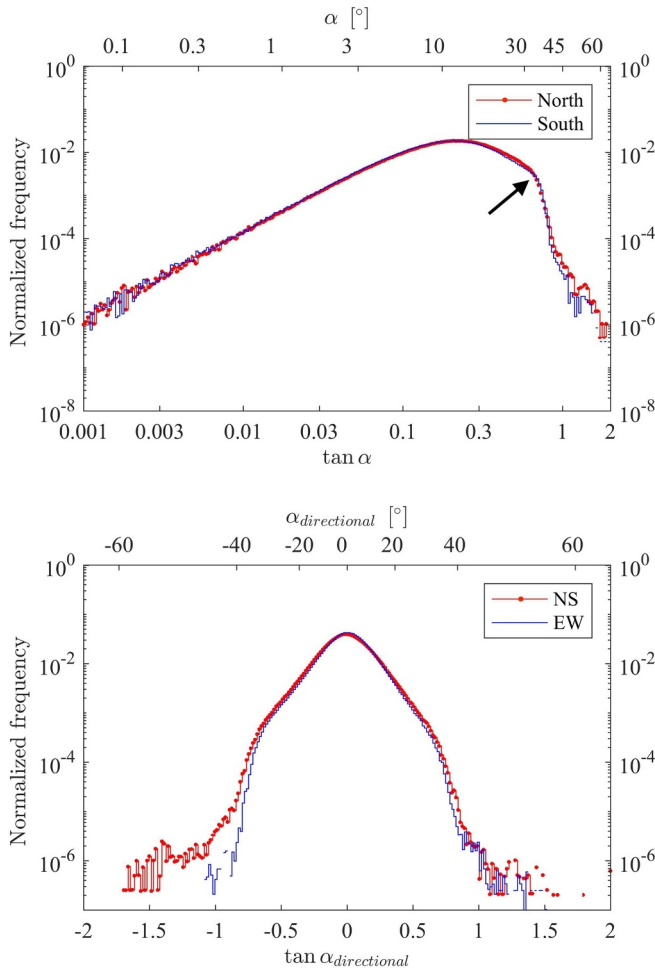
Fig. 10. Gravitational slope at Ahuna Mons. Ahuna Mons is centered at latitude of $-10.5°$ and longitude (eastward) of $-43.8°$ and is visible as a ring of red (marked by white arrows) that corresponds to the steep flanks. Another ring of red to the north of Ahuna Mons (marked by black arrows) is an unnamed crater. The contour lines are drawn for the slopes of 34° (yellow), 36° (green), 38° (blue). It can be seen that Ahuna Mons northern flank has a slope exceeding 36° with the maximum slope of 38°.

The gravitational potential can be defined as:

$$U(r, \lambda, \phi) = \frac{GM}{r} \sum_{n=1}^{\infty} \sum_{m=0}^{n} \left(\frac{R}{r}\right)^n \bar{P}_{nm}(\sin \phi)[\bar{C}_{nm} \cos(m\lambda) + \bar{S}_{nm} \sin(m\lambda)],$$

where $\bar{C}_{nm}$ and $\bar{S}_{nm}$ are the normalized gravity spherical harmonic coefficients. Table 5 shows the coefficients $\bar{C}_{nm}$ and $\bar{S}_{nm}$ up to degree 18 assuming Ceres is homogenous in density with gravitational constant of $GM = 62.62905$ km^3/s^2. These coefficients can be scaled using different upper-layer (i.e., crustal) density assumptions and combined with CERES18C to explore the interior structure of Ceres (Park et al., 2016; Ermakov et al., 2017; Konopliv et al., 2017). We note that the summation starts at $n = 1$ due to the offset between the center-of-mass and center-of-figure.

3.6. Surface slopes

Using the high-resolution, SPC-derived shape model, we have computed the total gravitational slope of Ceres, α, which is defined as the angle between the inward-pointing surface normal and the sum of the local gravity and centrifugal acceleration vectors. The local gravity direction was computed using the CERES18C gravity model truncated to degree and order 16 (Konopliv et al., 2017). Fig. 8(top) shows the total gravity slope in the Mollweide projection. As shown in the histogram in Fig. 9(top), the distributions of $\tan(\alpha)$ for the northern and southern hemispheres are nearly identical, indicating no hemispherical dichotomy. The histogram shows a steady increase of the frequency until a local maximum at $\alpha \approx 12°$ followed by a steady decrease. There is a kink in the histogram at $\alpha = 34.49°$ ($+0.02/-0.15$): at higher slopes, the histogram values abruptly go down. The kink was found by fitting a piecewise linear function to the histogram values. The confidence interval (16th and 84th percentile) were computed using bootstrapping. We hypothesize that this kink is likely due to reaching the angle of repose, i.e. the steepest angle at which loose material will not slump

Fig. 9. Top: histogram of the total gravity slope for the southern and northern hemisphere. The bins are uniformly spaced for the $\log_{10}(\tan(\alpha))$. The regions below 70°S and above 70°N were excluded due to insufficient image coverage in the southern hemisphere. The angle of repose at $\approx 34.5°$ is inferred from the kink in the histogram shown by the black arrow. Bottom: histogram of the North-South (red) and East-West (blue) directional slopes. Note that in the bottom histogram the horizontal axis has a linear scale, whereas in the top histogram the horizontal axis has a logarithmic scale.

degree-2 coefficients, the normalization factors are $N_{20} = \sqrt{5}$, $N_{21} = \sqrt{5/3}$, and $N_{22} = \sqrt{5/12}$.

We have computed the topography spherical harmonic coefficients up to $n = 2800$, which gives the half-wavelength resolution of about 500 m, using SHTOOLS (Wieczorek et al., 2016). Fig. 7 shows the root-mean-square of the topography spherical harmonic coefficients, i.e.,

$$RMS_n = \sqrt{\frac{\sum_{m=0}^{n} (\bar{A}_{nm}^2 + B_{nm}^2)}{2n + 1}},$$

which is often useful for geophysical interpretations, especially when combined with gravity spherical harmonics. For this reason, Table 4 shows the degree and order 18 topography spherical harmonic coefficients so that it's compatible with the degree and order 18 gravity field, called CERES18C, reported in Konopliv et al. (2017).

3.5. Gravity spherical harmonic coefficients

Similar to topography spherical harmonic coefficients discussed in Section 3.4, we have computed the gravity spherical harmonics from the SPC-derived topography of Ceres using SHTOOLS (Wieczorek et al., 2016) with the topography power of 15 (Wieczorek and Phillips, 1998).
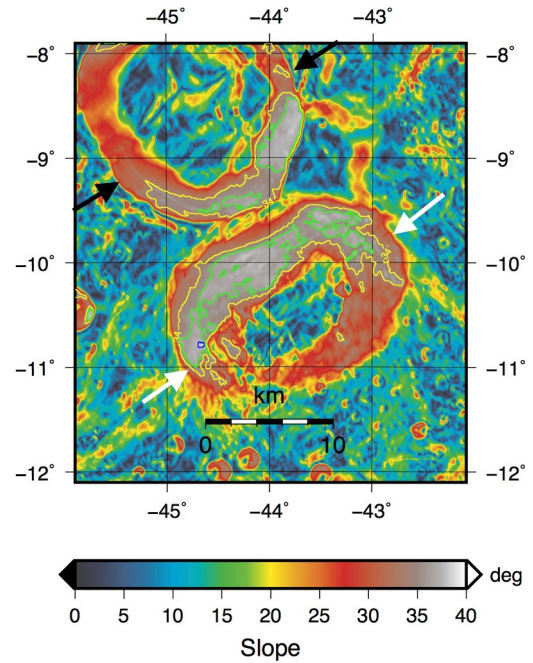
(see, for example, Melosh, 2011, Section 8.2.1). About 0.7% of Ceres' surface has $\alpha > 34.5°$, which, in most cases, corresponds to the steep crater walls exposing bedrock. One of the particularly steep regions is an isolated 17 km-wide and 4-km-high mountain called Ahuna Mons. This is the only positive topography feature of such size and morphology with gravitational slopes reaching or exceeding the estimated angle of repose. Fig. 10 shows the total gravitational slopes for Ahuna Mons. It can be seen that the maximum slope reached at the southwestern flank of Ahuna Mons is $\approx 38°$, which is over the globally averaged angle of repose inferred from the kink in the histogram. This may indicate either that the Ahuna Mons material, if it is loose, might have a higher coefficient of internal friction; or that consolidated bedrock is exposed at the flanks of Ahuna Mons. The more coherent, mechanically strong material may suggest that the mons is relatively young, i.e., not mechanically weakened by micrometeorite impacting, and consistent with crater-based age determination (Ruesch et al., 2016).

We have also computed bidirectional (i.e., North-South and East-West) gravitational slopes. The North-South and East-West slopes are defined by the angles between the projections of the two vectors used to compute the total gravity slope onto the planes of the local meridian and prime vertical, respectively. Based on this definition, positive North-South (East-West) slope would indicate South-facing (West-facing) slope. For example, zero North-South slope would mean the direction of the steepest descent is either East or West and zero East-West slope would mean that the direction of the steepest descent is either North or South. Alternatively, a 90°-slope would correspond to a vertical cliff. Fig. 8(middle) and Fig. 8(bottom) show the Mollweide projection of North-South and East-West slopes, respectively. The bidirectional gravity slopes can be used to determine the downhill direction, which could aid geologic mapping and analysis of flow features. Additionally, Fig. 9(bottom) shows the distributions of the North-South and East-West slopes. The distributions are zero-mean, symmetric and nearly identical as expected for isotropic topography.

4. Conclusions

This paper presented a high-resolution global shape model of Ceres determined using a stereophotoclinometry technique by processing Dawn's Framing Camera images (i.e., 93.7 µrad per pixel) acquired during Approach to post-LAMO phases. About a total of 38,000 clear-filter images were processed with image pixel scales ranging from 35.6 km to 35 m. Detailed error analysis showed that the average total topography height error is 10.2 m and about 88.9% of the surface had a total topography height error below 20 m. We also made improved estimates of global parameters, such as the *GM*, pole right ascension, pole declination, prime meridian and rotation rate.

Using the global shape model, the resulting volume of Ceres is $(434.13 \pm 0.50) \times 10^6$ km^3 with a volumetric mean radius of 469.72 km. Combined with the mass estimate, the resulting bulk density is (2161.6 ± 2.5) kg/m^3. The vector from the center-of-mass to center-of-figure is $(-0.893, -0.379, 0.351) \pm 0.015$ km, or with magnitude of (1.031 ± 0.015) km, in the Ceres body-fixed coordinate system and the best-fit ellipsoid has the principal semi-axes of (483.21, 481.00, 445.93) km. Lastly, we provided spherical harmonic coefficients and a gravitational slope map for geophysical and geological studies.

Acknowledgments

Supplementary materials

Supplementary material associated with this article can be found, in the online version, at doi:10.1016/j.icarus.2018.10.024.

References

Buczkowski, D.L., Wyrick, D.Y., Iyer, K.A., Kahn, E.G., Scully, J.E.C., Nathues, A., Gaskell, R.W., Roatsch, T., Preusker, F., Schenk, P.M., Le Corre, L., Reddy, V., Yingst, R.A., Mest, S., Williams, D.A., Garry, W.B., Barnouin, O.S., Jaumann, R., Raymond, C.A., Russell, C.T., 2012. Large-scale troughs on Vesta: a signature of planetary tectonics. Geophys. Res. Lett. 39, L18205. https://doi.org/10.1029/2012GL052959.

Chamberlain, M.A., Sykes, M.V., Esquerdo, G.A., 2007. Ceres lightcurve analysis – period determination. Icarus 188, 451–456. https://doi.org/10.1016/j.icarus.2006.11.025.

Ermakov, A.I., Fu, R.R., Castillo-Rogez, J.C., Raymond, C.A., Park, R.S., Preusker, F., Russell, C.T., Smith, D.E., Zuber, M.T., 2017. Constraints on Ceres' internal structure and evolution from its shape and gravity measured by the Dawn spacecraft. J. Geophys. Res. Planets 122, 2267–2293. https://doi.org/10.1002/2017JE005302.

Evan, S., Taber, W., Drain, T., Smith, J., Wu, H.-C., Guevara, M., Sunseri, R., Evans, J., 2018. MONTE: the next generation of mission design and navigation software. CEAS Space J. 10, 79–86. https://doi.org/10.1007/s12567-017-0171-7.

Fairbairn, M.B., 2005. Planetary Photometry: the Lommel–Seeliger law. J. R. Astron. Soc. Can. 99, 92.

Fu, R.R., Ermakov, A.I., Marchi, S., Castillo-Rogez, J.C., Raymond, C.A., Hager, B.H., Zuber, M.T., King, S.D., Bland, M.T., De Sanctis, M.C., Preusker, F., Park, R.S., Russell, C.T., 2017. The interior structure of Ceres as revealed by surface topography. Earth Planet. Sci. Lett. 476, 153–164.

Gaskell, R.W., 2005. Landmark navigation and target characterization in a simulated Itokawa encounter. In: AAS/AIAA Astrodynamics Specialists Conference. Lake Tahoe, California, USA. AAS paper 05-289.

Gaskell, R.W., Barnouin-Jha, O.S., Scheeres, D.J., Konopliv, A.S., Mukai, T., Abe, S., Saito, J., Ishiguro, M., Kubota, T., Hashimoto, T., Kawaguchi, J., Yoshikawa, M., Shirakawa, K., Kominato, T., Hirata, N., Demura, H., 2008. Characterizing and navigation small bodies with imaging data. Meteorit. Planet. Sci. 43 (6), 1049–1061.

Hapke, B., 1981. Bidirectional reflectance spectroscopy: 1. theory. J. Geophys. Res. Solid Earth 86 (B4), 3039–3054.

Konopliv, A.S., Asmar, S.W., Bills, B.G., Mastrodemos, N., Park, R.S., Raymond, C.A., Smith, D.E., Zuber, M.T., 2011. The Dawn gravity investigation at Vesta and Ceres. Space Sci. Rev. 163, 461–486. https://doi.org/10.1007/s11214-011-9794-8.

Konopliv, A.S., Asmar, S.W., Park, R.S., Bills, B., Centinello, F., Chamberlin, A.B., Ermakov, A., Gaskell, R.W., Rambaux, N., Raymond, C.A., Russell, C.T., Smith, D.E., Tricarico, P., Zuber, M.T., 2014. The Vesta gravity field, spin pole and rotation period, landmark positions, and Ephemeris from the Dawn tracking and optical data. Icarus 240, 103–117. https://doi.org/10.1016/j.icarus.2013.09.005.

Konopliv, A.S., Park, R.S., Vaughan, A.T., Bills, B.G., Asmar, S.W., Ermakov, A.I., Rambaux, N., Raymond, C.A., Castillo-Rogez, J.C., Russell, C.T., Smith, D.E., Zuber, M.T., 2017. The Ceres gravity field, spin pole, rotation period and orbit from the Dawn radiometric tracking and optical data. Icarus 299, 411–429.

McEwen, A.S., 1986. Exogenic and endogenic albedo and color patterns on Europa. J. Geophys. Res. 91 (B8), 8077–8097.

Melosh, H.J., 2011. Planetary Surface Processes 13. Cambridge University Press, pp. 512.

Mohr, P.J., Taylor, B.N., Newell, D.B., 2012. CODATA recommended values of the fundamental physical constants: 2010. Rev. Mod. Phys. 84, 1527–1605.

Mohr, P.J., Newell, D.B., Taylor, B.N., 2016. CODATA recommended values of the fundamental physical constants: 2014. Rev. Mod. Phys. 88, 035009.

Moyer, T.D., 1971. Mathematical Formulation of the Double-Precision Orbit Determination Program (DPODP). Jet Propulsion Laboratory, California Institute of Technology, Pasadena, CA JPL Technical Report 32-1527.

Moyer, T.D., 2000. Formulation for Observed and Computed Values of Deep Space Network Data Types for navigation, Monograph 2 of Deep Space Communications and Navigation Series. JPL Publication 00-7. Jet Propulsion Laboratory, California Institute of Technology, Pasadena, CA.

Nathues, A., Platz, T., Thangjam, G., Hoffmann, M., Mengel, K., Cloutis, E.A., Le Corre, L., Reddy, V., Kallisch, J., Crown, D.A., 2017. Evolution of Occator Crater on (1) Ceres. Astron. J. 153, 112 (12pp).

Park, R.S., Konopliv, A.S., Asmar, S.W., Bills, B.G., Gaskell, R.W., Raymond, C.A., Smith, D.E., Zuber, M.T., 2014. Gravity field expansion in ellipsoidal harmonic and polyhedral internal representations applied to Vesta. Icarus 240, 118–132. https://doi.org/10.1016/j.icarus.2013.12.005.

Park, R.S., Bills, B.G., Buffington, B.B., Folkner, W.M., Konopliv, A.S., Marti-Mur, T.J., Mastrodemos, N., McElrath, T.P., Riedel, J.E., Watkins, M.M., 2015. Improved detection of tides at Europa with radiometric and optical tracking during flybys. Planet. Space Sci. 112, 10–14.

Park, R.S., Konopliv, A.S., Bills, B.G., Rambaux, N., Castillo-Rogez, J.C., Raymond, C.A., Vaughan, A.T., Ermakov, A.I., Zuber, M.T., Fu, R.R., Toplis, M.J., Russell, C.T., Nathues, A., Preusker, F., 2016. A partially differentiated interior for Ceres deduced from its gravity field and shape. Nature 537, 515–517. https://doi.org/10.1038/nature18955.

Preusker, F., Scholten, F., Matz, K.-D., Elgner, S., Jaumann, R., Roatsch, T., Joy, S.P., Polanskey, C.A., Raymond, C.A., Russell, C.T., 2016. Dawn at Ceres - shape model and rotational state. LPSC Meeting Abstract 1954.

Rayman, M.D., Fraschetti, T.C., Raymond, C.A., Russell, C.T., 2006. Dawn: a mission in development for exploration of main belt asteroids Vesta and Ceres. Acta Astronaut. 58, 605–616.

Raymond, C.A., Jaumann, R., Nathues, A., Sierks, H., Roatsch, T., Preusker, F., Scholten, F., Gaskell, R.W., Jorda, L., Keller, H.-U., Zuber, M.T., Smith, D.E., Mastrodemos, N., Mottola, S., 2011. The Dawn Topography investigation. Space Sci. Rev. 163 (1), 487–510.

Roatsch, T., E., K., K.-D., M., F., P., F., S., S., E., S.E., S., R., J., C.A., R., C.T., R., 2016a. Dawn FC2 Derived Ceres HAMO DTM SPG V1.0, DAWN-A-FC2-5-CERESHAMODTMSPG-V1.0. NASA Planetary Data System.

Roatsch, T., E., K., K.-D., M., F., P., F., S., R., J., C.A., R., C.T., R., 2016b. Corrigendum to "Ceres survey atlas derived from Dawn Framing Camera images. Planet Space Sci. 121 (2016), 115–120 145, 78-79.

Ruesch, O., Platz, T., Schenk, P., McFadden, L.A., Castillo-Rogez, J.C., Quick, L.C., Byrne, S., Preusker, F., O'Brien, D.P., Schmedemann, N., Williams, D.A., Li, J.-Y., Bland, M.T., Hiesinger, H., Kneiss, T., Neesemann, A., Schaefer, M., Pasckert, J.H., Schmidt, B.E., Buczkowski, D.L., Sykes, M.V., Nathues, A., Roatsch, T., Hoffmann, M., Raymond, C.A., Russell, C.T., 2016. Cryovolcanism on Ceres. Science 353 (6303). https://doi.org/10.1126/science.aaf4286.

Russell, C.T., Capaccioni, F., Coradini, A., Christensen, U., De Sanctis, M.C., Feldman, W.C., Jaumann, R., Keller, H.U., Konopliv, A., McCord, T.B., McFadden, L.A., McSween, H.Y., Mottola, S., Neukum, G., Pieters, C.M., Prettyman, T.H., Raymond, C.A., Smith, D.E., Sykes, M.V., Williams, B., Zuber, M.T., 2006. Dawn discovery mission to Vesta and Ceres: present status. Adv. Space Res. 38, 2043–2048.

Schröder, S.E., Mottola, S., Carsenty, U., Ciarniello, M., Jaumann, R., Li, R.J.-Y., Longobardo, A., Palmer, E., Pieters, C., Preusker, F., Raymond, C.A., Russell, C.T., 2017. Resolved spectrophotometric properties of the Ceres surface from Dawn Framing Camera images. Icarus 288, 201–225.

Sierks, H., Keller, H.U., Jaumann, R., Michalik, H., Behnke, T., Bubenhagen, F., Büttner, I., Carsenty, U., Christensen, U., Enge, R., Fiethe, B., Gutiérrez Marqués, P., Hartwig, H., Krüger, H., Kühne, W., Maue, T., Mottola, S., Nathues, A., Reiche, K.-U., Richards, M.L., Roatsch, T., Schröder, S.E., Szemerey, I., Tschentscher, M., 2011. The Dawn Framing Camera. Space Sci. Rev. 163 (1), 263–327.

Squyres, S.W., Veverka, J., 1982. Variation of albedo with solar incidence angle on planetary surfaces. Icarus 50 (1), 115–122.

Thomas, P.C., Wm. Parker, J., McFadden, L.A., Russell, C.T., Stern, S.A., Sykes, M.V., Young, E.F., 2005. Differentiation of the asteroid Ceres as revealed by its shape. Nature 437, 224–226.

Wieczorek, M.A., Phillips, R.J., 1998. Potential anomalies on a sphere: applications to the thickness of the lunar crust. J. Geophys. Res. 103 (E1), 1715–1724.

Wieczorek, M.A., Mesch, M., de Andrade, E.S., Oshchepkov, I., and heroxbd (2016), SHTOOLS/SHTOOLS: Version 4.0, 10.5281/zenodo.206114.